SUPPORTING INFORMATION FOR "SHAPE-MORPHING ARCHITECTED SHEETS WITH NON-PERIODIC CUT PATTERNS"

SPECIMEN FABRICATION

A Universal ILS9 120W laser cutter is used to create perforations. We mainly use 1.55 mm-thick natural rubber sheets (McMaster-Carr, item no. 8633K71), but some 3.1 mm- and 0.75 mm-thick ones were also used (Grainger, items no. 1XWE5 and 8611K18). For the 1.55 mm-thick specimens, the machine is set to cut at 35% power and 5% speed, with an air assist flow rate of 100% to avoid burning the specimens. For the 3.1 mm-thick specimens, 45% power and 2.3% speed are selected. For the 0.75 mm-thick specimens, 30% power and 5% speed are selected. Since the laser beam has a finite cutting diameter, the hinges are not characterized by sharp corners but are de-facto beams having a finite length. The tube specimens are closed using double-sided tape glued to some tiles. PETG sheets (0.5 mm-thick) were perforated with the same laser cutter, with 3.0% power and 2.2% speed, and were also closed into surfaces of revolution using double-sided tape.

ADDITIONAL INFORMATION ON THE TENSILE TESTS

Uniaxial tensile tests are conducted using an Instron ElectroPuls (Model E3000) system equipped with a 250 N load cell at a constant deformation rate of $2\,\mathrm{mm\,s^{-1}}$. The tensile forces and displacements are measured with 1 mN and $5\,\mu$m accuracy, respectively, at an acquisition rate of 1 kHz. The force-displacement data obtained from the Instron WaveMatrix software is converted to stress-stretch data using the original sample dimensions. The data obtained is then subsampled to remove some of the noise (one every 10 measurements is kept). The response of the specimen in Fig. 1(a) is replicated in Fig. S1, where the insets represent a few stages of the deformation of the specimen and show the experimental setup. To accomodate lateral expansions and/or contractions of the specimens undergoing tensile

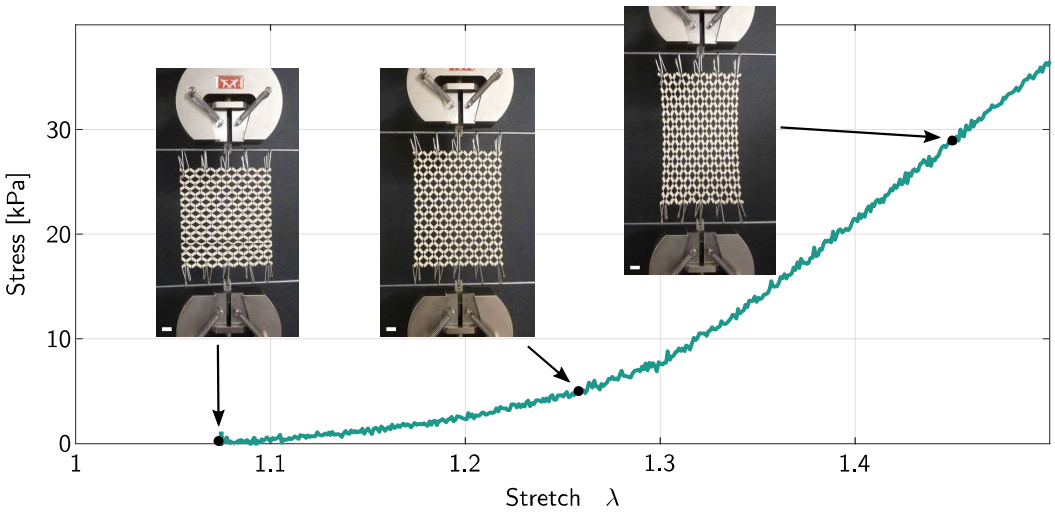

FIG. S1. Response of a 18×18 tile, anisotropic sheet with $\delta/l_x = 1/8$ and $t/l_x \sim 0.26$. The insets depict the experimental setup and the response at three stretch values. (Scale bar, 12 mm)

loads, we employ a fixture where specimens are hung in a curtain-like fashion. We use 3D-printed parts (Formlabs Form 2, clear resin) to connect horizontal steel rods to the Instron's clamps; we then use paper clips as "hooks" to hang the specimens (at 5 locations on each side). Upon pulling, the paper clips can slide on the steel rod; the friction between these components will inevitably affect the response. Note that, due to the very small forces involved in our experiments, we claim that the elasticity of paper clips and steel rods only minimally affects the response. From Fig. S1, we see that the response is recorded only for values of stretches larger than ~ 1.08. This is due to the fact that, when attached to our fixtures, some of the sheets we consider tend to deform due to their self weight. This self-stretching happens only when specimens feature mechanism-like deformation in the pulling direction. For example, in Fig. 1(a), the curve corresponding to horizontal stretching starts at 1.08, while the one for vertical stretching starts at 0.

From Fig. 1(a), we can see that the slopes of the elasticity-dominated portions of the experimental curves corresponding to horizontal and vertical stretching are not identical. This is caused by the fact that the size of the vertical and horizontal hinges in our anisotropic specimens are not identical. This is clearly visible from Fig. S2. In particular,

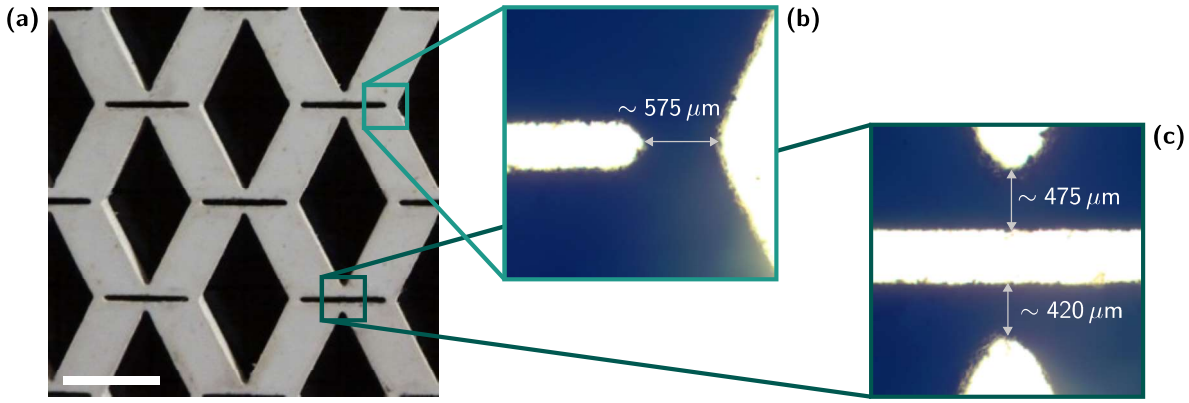

FIG. S2. (a) Detail of one of the anisotropic architectures analyzed in this work (Scale bar, 6 mm). (b) and (c) Microscope images (2.5× zoom) representing the details of vertical and horizontal hinges, respectively.

the laser cutting process causes vertical hinges to be thicker than the horizontal ones. This explains why in Fig. 1(a) the continuous light gray curve is steeper than the elasticity-dominated portion of the continuous black curve.

In Fig. S8 we report the tensile response of the isotropic auxetic architecture displayed in Fig. 1(c) and Fig. S5(a). The two continuous lines, dark and light, represent the experimental curves obtained by pulling the specimen along

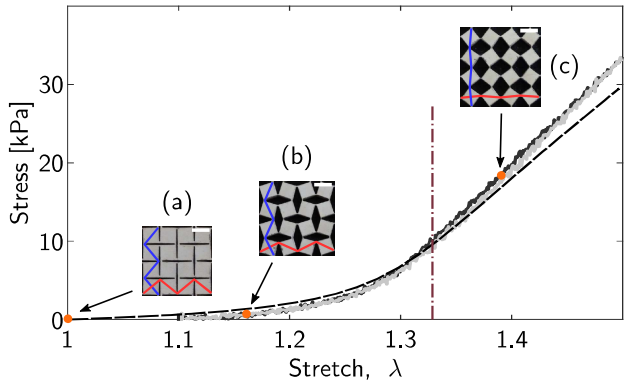

FIG. S3. Tensile response of a periodic sheet featuring the undeformed architecture in (a). Black lines represent the sheet's response to horizontal stretching and light gray lines to vertical stretching. Solid lines are experimental curves. The dashed line represent the numerical response to both horizontal and vertical loading. The vertical dash-dot line shows the theoretically-predicted value for the transition from a mechanism-dominated deformation to an elastic deformation. Insets (a-c) show different stages of the sheet's deformation (Scale bar, 6 mm); the red and blue lines highlight the diagonals of each tile in a given row and column, respectively.

the horizontal and vertical directions, respectively. The two almost overlap, as expected, due to the isotropic nature of the specimen's response. The dashed line is obtained from FE simulations. The superimposed dash-dot curve represents the analytical mechanism-to-elasticity transition.

DETAILS ON THE FINITE ELEMENT MODEL

In this work, finite element simulations are carried out using Abaqus/Standard. The investigated sheets present different lengthscales: the hinge in-plane width and length ($\sim 1\,\mathrm{mm}$), the length of a tile ($\sim 10\,\mathrm{mm}$), and the total size of the sheet ($\sim 100\,\mathrm{mm}$). Since the mechanical behavior of the sheets is, to a large extent, governed by the design of the hinges, a sufficiently fine mesh is required to accurately capture the correct response. Another challenge stems from the large nonlinearities involved and from the large distortions happening at large stretches. In order to efficiently identify regions that are prone to out-of-plane bending, we conduct two-dimensional finite element simulations. In all simulations, we resort to a plane strain assumption, accounting for the fact that the response is primarily determined by the hinge dimensions, and the hinges' in-plane width ($\sim 0.5\,\mathrm{mm}$) is smaller than their out-of-plane thickness ($\sim 1.55\,\mathrm{mm}$). Throughout this work, we consider geometric nonlinearities and model the nonlinear material behavior of natural rubber gum with a Neo-Hookean material model. This model is fit to the experimental response of a natural rubber dogbone specimen to tensile loading. Fig. S4(a) shows a detail of the mesh at one of the hinges. We

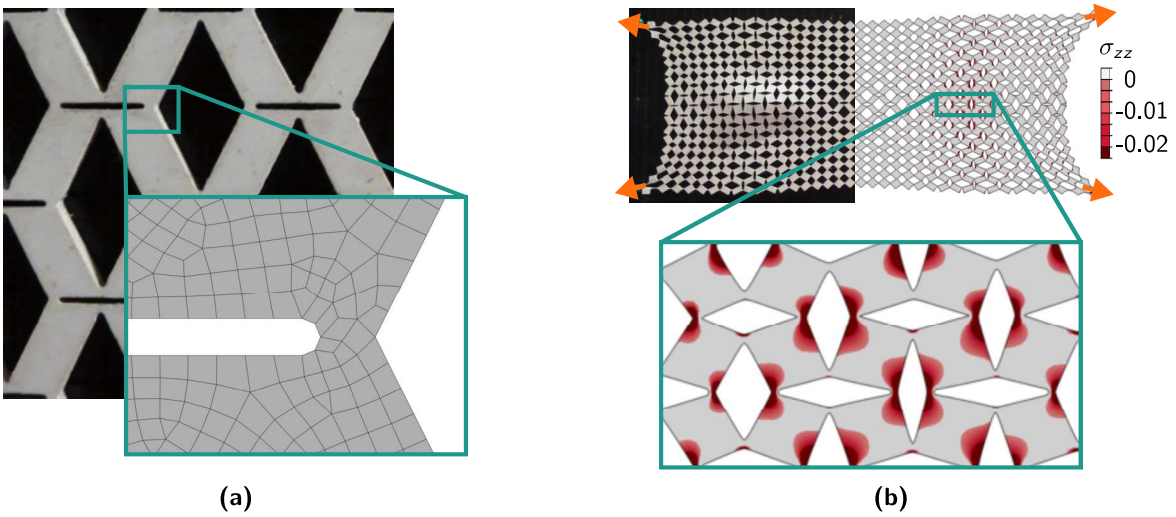

FIG. S4. Details of the FE model. (a) Detail of the mesh used for one of the hinges in the simulation of the anisotropic specimen tensile test. (b) Detail of the stress map for the simulation in Fig. 3(a2).

check mesh convergence for one of the simulations used to obtain the numerical curves in Fig. 1(a). We change the element size and monitor the stress values recorded for a given stretch along a given direction. The errors we obtain for doubling the average element size are below 0.73%.

The results reported in Fig. 1(a) and Fig. S3 show that the numerics capture the features observed experimentally, even though some discrepancies between experiments and numerics arise at large stretches. These discrepancies can be attributed to several factors: 1) the inability of the Neo-Hookean model to capture the correct mechanical behavior at large stretches; 2) the fact that the CAD models used for our numerical simulations do not account for the exact hinge dimension that results from the laser cutting process; 3) the simulated loads might not be exactly identical to the experimental ones.

The stress maps in Fig. 3 represent the out-of-plane stress $\sigma_z = \nu(\sigma_x + \sigma_y)$. The colormap is designed to give relevance only to compressive stresses—those that are responsible for the onset of buckling. The stresses are not averaged over subdomains. Thus, the red areas in Fig. S4(b) correspond to the compressive stress of the hinges. We also observe that the compressive stresses partially percolate into the tiles. This is likely responsible for out-of-plane buckling. From Fig. 3(b2-b3), we can see that the stress maps for the two loading configurations are almost identical. For this reason, the stress maps do not contain enough information to determine the exact shape of the resulting buckling patterns in complex scenarios, but give a useful guideline on where buckling is likely to occur in simple cases like that depicted in Fig. 3(a1-a2).

KINEMATIC ANALYSIS

The sheets discussed in this work are designed to display mechanisms of inextensional deformation, i.e., low energy modes of compliant mechanism-like deformation. In this Section, we consider the pin-jointed truss analogs of some of our sheets, and resort to the matrix analysis detailed by Pellegrino & Calladine [49] and Hutchinson & Fleck [51] to determine what these mechanisms are. This analysis consists of the following steps. First, we calculate the equilibrium matrix $\mathbf{A}$, that relates bar tensions $\mathbf{t}$ and joint forces $\mathbf{f}$ according to $\mathbf{A} \cdot \mathbf{t} = \mathbf{f}$, and the kinematic matrix $\mathbf{B}$, relating joint displacements $\mathbf{d}$ and bar elongations $\mathbf{e}$ according to $\mathbf{B} \cdot \mathbf{d} = \mathbf{e}$. Note that equilibrium imposes that $\mathbf{B} = \mathbf{A}^{\mathrm{T}}$. Then, we apply boundary conditions to suppress rigid body motions; in this case, we block the x and y displacements of node (1,1), the node at the bottom left of the specimen, and the y displacement of node (2,1). Finally, we compute the null space of $\mathbf{B}$. If the system is properly constrained, each vector belonging to this null space represents a mode of inextensional deformation. The results of this analysis for two cut patterns are shown in Fig. S5. First, we consider the

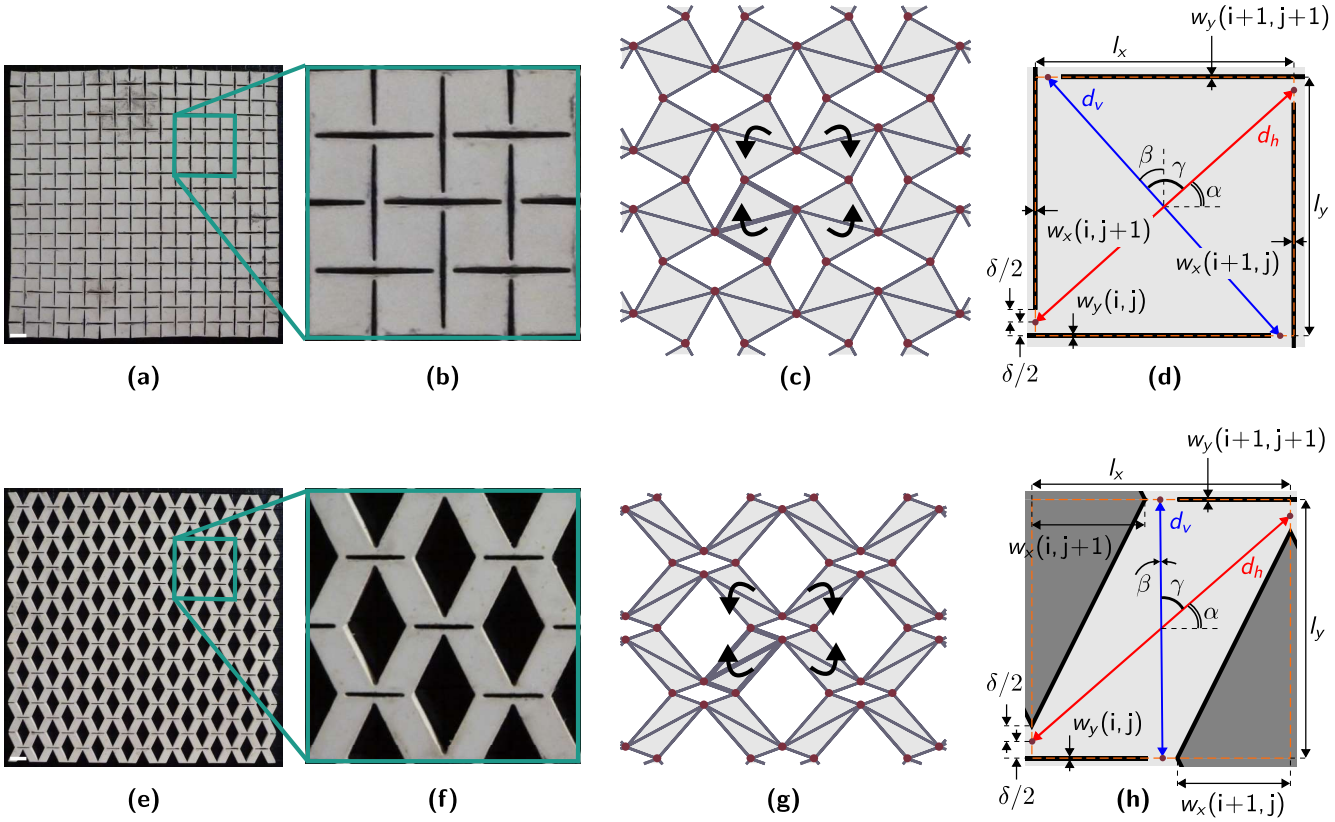

FIG. S5. Kinematic analysis of periodic perforated sheets featuring tiles connected by thin hinges. (a) Isotropic sheet and (b) detail. (c) Mechanism of inextensional deformation for the truss analog of (a), obtained by computing the null space of the kinematic matrix. (d) Detail of one of the tiles of (a), indicating all the quantities necessary for the kinematic analysis. (e-h) Same as (a-d), but for the architecture in (e). (Scale bar, 6 mm)

periodic architecture in Fig. S5(a-b), known for its auxeticity [4]. The matrix analysis of the pin-jointed truss analog to this system predicts only one mechanism, shown in Fig. S5(c), and characterized by the tile rotations highlighted by the black arrows. Note that this geometry features no states of self-stress. Thus, even though the analysis assumes small deformations, the same mechanism should extend to large stretch regimes [51]. The periodic sheet in Fig. S5(e) (same as the one shown in Fig. 1(a)) features a very similar mechanism of inextensional deformation, characterized by the same relative rotations of the tiles, but with an equivalent positive Poisson's ratio. The tensile tests in Fig. 1(a) demonstrate that the rubber sheets, despite presenting non-idealities such as finite-sized hinges, deform according to the corresponding mechanisms up to certain stretch values.

Knowing how these periodic sheets deform in plane, we resort to a kinematic model in order to quantify their mechanism-like deformation. The unit cells for these periodic architectures consist of four adjacent tiles. It is sufficient to consider a single tile to determine the whole system's response. In Fig. S5(d,h) we show a single tile from the sheets in Fig. S5(a,e), such that $(i+j)/2 \in \mathbb{Z}$, and we indicate all the useful geometric parameters. Here,

$(i,\, j)$ indicates a generic tile, with $i = 1, ..., N_x + 1$, $j = 1, ..., N_y + 1$ and N_x, N_y being the number of tiles along the horizontal and vertical directions. Note that, if we consider a tile such that $(i+j)/2 \notin \mathbb{Z}$, the following formulae will only slightly vary. For the remainder of this section, we assume that we are dealing with periodic architectures; this implies that $w_y(i,j) = w_y(i+1, j+1) = w_y$, and $w_x(i+1, j) = w_x(i, j+1) = w_x$. The red and blue lines indicate the diagonals of each tile. Their lengths are

$$d_h = \sqrt{l_x^2 + [l_y - 2w_y - \delta]^2} \quad \text{and} \quad d_v = \sqrt{l_y^2 + [l_x - 2w_x - \delta]^2}\,. \tag{S2}$$

Ideally, tiles can rotate until the diagonal lines corresponding to the selected stretch direction are straightened. With this in mind, we can determine the maximum horizontal and vertical stretches for any periodic architecture designed following our paradigm, as

$$\lambda_x^M = \frac{d_h}{l_x} \quad \text{and} \quad \lambda_y^M = \frac{d_v}{l_y}\,. \tag{S3}$$

We can also use kinematics to derive formulae for the tangential stretches as functions of λ_x^M or λ_y^M. First, we determine the angle α between d_h and the x-axis in the undeformed configuration, and β between d_v and the y-axis, as

$$\alpha = \arctan\left(\frac{l_y - 2w_y - \delta}{l_x}\right) \quad \text{and} \quad \beta = \arctan\left(\frac{2w_x + \delta - l_x}{l_y}\right)\,. \tag{S4}$$

Note that we define α to be positive counterclockwise and β to be positive clockwise. We also define $\gamma = \pi/2 - \alpha - \beta$ as the angle between d_h and d_v. During mechanism-like deformation, γ remains fixed since we assume the tiles are rotating rigidly. On the other hand, the inclinations of d_h and d_v with respect to x and y change during the deformation process. To determine the intermediate stages of the sheet's deformation, we define α^* and β^* as angles varying from 0 to α and 0 to β, respectively. Consider now the case of stretching along x. We can write

$$\lambda_x(\alpha^*) = \frac{d_h \cos\alpha^*}{l_x} \quad \text{and} \quad \lambda_y(\alpha^*) = \frac{d_v \sin(\gamma + \alpha^*)}{l_y}\,. \tag{S5}$$

From the first of the two equations, we obtain $\alpha^*(\lambda_x)$ as

$$\alpha^*(\lambda_x) = \arccos\left(\frac{\lambda_x l_x}{d_h}\right)\,. \tag{S6}$$

Substitution leads to the following formula for $\lambda_y(\lambda_x)$:

$$\lambda_y(\lambda_x) = \frac{d_v}{l_y} \sin\left[\gamma + \arccos\left(\frac{\lambda_x l_x}{d_h}\right)\right]\,. \tag{S7}$$

This formula is used to determine the analytical curves in Fig. 1(f), representing the evolution of the tangential stretch as a function of the applied one. Note that a similar formula can be obtained for $\lambda_x(\lambda_y)$.

In our work, we fix the design parameters l_x, l_y and δ most of the time, and vary w_x and w_y. Different combinations of w_x and w_y allow to span a wide design space in terms of achievable deformations. To get a better idea of the available design space, in Fig. S6, we report plots for the maximum stretch λ_x^M, and the related tangential stretch $\lambda_y(\lambda_x^M)$, as a function of w_x and w_y. Note that the values in the colormaps are specific for $l_x = l_y = 6\,\text{mm}$ and $\delta = l_x/8$. We can see that choosing w_x and w_y allows to obtain a wide range of responses to stretching. Some significant examples (A, B, C and D) are extracted from the design space. A, corresponding to $w_x = w_y = 0$, is characterized by $\lambda_x^M = \lambda_y(\lambda_x^M) = 1.33$; B, corresponding to $w_x = (l_x - \delta)/2$ and $w_y = 0$, is characterized by $\lambda_x^M = 1.33$ and $\lambda_y(\lambda_x^M) = 0.75$; C, corresponding to $w_x = (l_x - \delta)/2$ and $w_y = (l_y - \delta)/2$, is kinematically undeformable albeit featuring bulky tiles connected by thin hinges; D, corresponding to $w_x = l_x - \delta$ and $w_y = 0$, does not behave like a mechanism since the rigid tiles assumption does not hold for these specific parameters. From these examples, it is clear that not all the configurations available in the design space allow to obtain the in-plane mechanism-like deformation behavior we are interested in. Therefore, particular care is needed when choosing the design parameters; in light of this, in this work, we limit ourselves to the ranges $0 \le w_x \le (l_x - \delta)/2$ and $0 \le w_y \le (l_y - \delta)/2$.

An example of non-periodic sheet is shown in Fig. S7(a). Non-periodicity leads to frustration and to the disappearance of mechanisms of inextensional deformation. This is confirmed by the matrix analysis of the pin-jointed

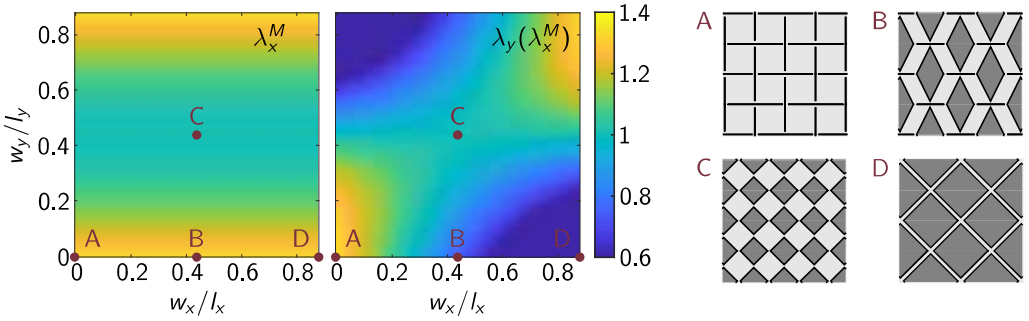

FIG. S6. Design space in terms of maximum stretches, λ_x^M and $\lambda_y(\lambda_x^M)$, as a function of w_x and w_y, with $l_x = l_y = 6\,\text{mm}$ and $\delta = l_x/8$ fixed. Insets A-D represent specific examples extracted from the space.

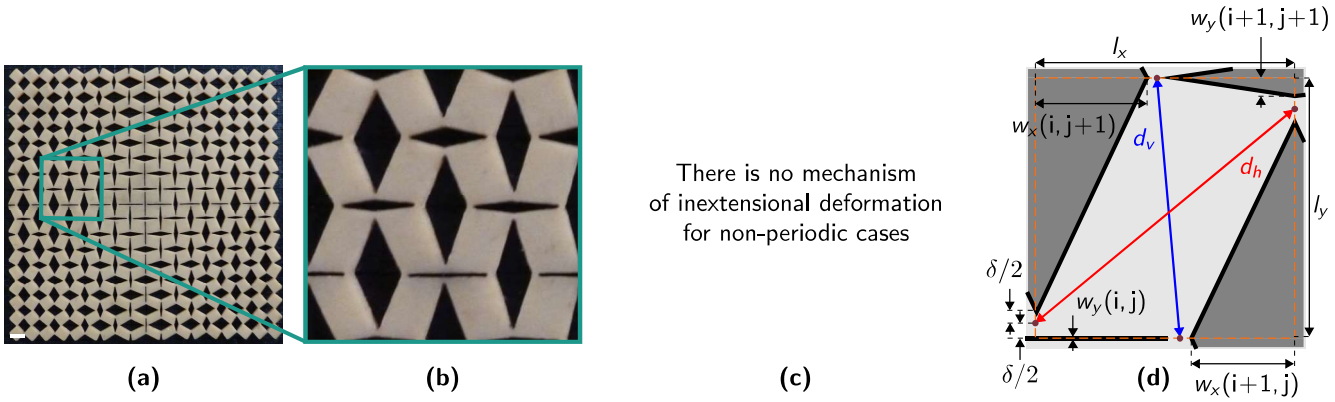

FIG. S7. Kinematic analysis of non-periodic perforated sheets featuring tiles connected by thin hinges. (a) Example of non-periodic sheet. (b) Detail of the sheet in (a). (c) The null space of the kinematic matrix of the pin-jointed truss analog to (a) contains no mechanism. (d) Detail of one of the tiles of the sheet in (a), with all the quantities necessary for the kinematic analysis. (e-h) Same as (a-d), but for the architecture in (e). (Scale bar, 6 mm)

truss analog of the architecture in Fig. S7(a), that has no mechanisms. In these non-periodic cases, we can still use kinematics to infer something about the local deformation of the sheet, even though it cannot be used to quantify global deformations as it did in periodic scenarios. For this reason, in the main article, we sometime consider the maximum stretches that a tile belonging to a non-periodic sheet can undergo. We interpret these stretches as measures of a local ability to deform. The local ability to behave like a mechanism is what makes these systems buckle out of plane. For a generic tile in a non-periodic scenario, whose bottom-left gridpoint (i, j) is such that $(i + j)/2 \in \mathbb{Z}$, the maximum stretches are calculated as in Eq. S3, with d_h and d_v computed as

$$d_h = \sqrt{l_x^2 + [l_y - w_y(i,j) - w_y(i+1,j+1) - \delta]^2} \quad \text{and} \quad d_v = \sqrt{l_y^2 + [l_x - w_x(i,j+1) - w_x(i+1,j) - \delta]^2}\,. \tag{S8}$$

CUT PATTERN GENERATION

Our cut patterns are generated and kinematically analyzed using custom MATLAB scripts. The first step of the design process is to generate a grid of points. The grid can be non-Cartesian, as long as it can be mapped to a rectangular one. At each grid point (i, j) with $i = 1, ..., N_x + 1$ and $j = 1, ..., N_y + 1$ with N_x and N_y being the number of tiles along the horizontal and vertical directions, we cut a diamond-shaped hole. For each diamond, we define either its horizontal or vertical half-diagonal, i.e. w_x or w_y. If $(i+j)/2 \in \mathbb{Z}$ we define the diamond's y-oriented half-diagonal $w_y(i, j)$. Its x-dimension will be determined by the neighboring diamonds—$l_x - \delta - w_x(i-1, j)$ to the left and $l_x - \delta - w_x(i+1, j)$ to the right of the grid point. Otherwise, if $(i + j)/2 \notin \mathbb{Z}$, we define $w_x(i, j)$ while the diamond's y-dimension follows from the neighboring diamonds. This design paradigm guarantees geometric continuity and that no perforations overlap, even in non-periodic architectures where we let w_x and w_y vary (smoothly or not) from diamond to diamond. In the case of architectures designed to allow for plastic deformations, instead of defining a diamond, we define an octahedron at each gridpoint.

The w_x, w_y functions corresponding to all cut patterns shown throughout this manuscript are listed in the following.

- "Anisotropic" sheet.
  Appearing in Fig. 1(a,d), Fig. S5(e), Fig. S4(a), Fig. S6B, Fig. S1, Fig. S2, Fig. S8.
  Loading: Uniform horizontal or uniform vertical.
  Material: Natural rubber gum of various thicknesses (1.55, 3.1 mm).
  Parameters: $N_x = N_y = 18$, $l_x = l_y = 6\,\text{mm}$, $\delta = l_x/8$.
  Hole size distribution (with $i = 1, ..., N_x + 1$, $j = 1, ..., N_y + 1$):

$$w_x(i, j) = (l_x - \delta)/2 \ , \quad w_y(i, j) = 0 \ .$$

- "Isotropic" sheet.
  Appearing in Fig. 1(c), Fig. S5(a), Fig. S6A, Fig. S3.
  Loading: Uniform horizontal or uniform vertical.
  Material: Natural rubber gum, 1.55 mm thick.
  Parameters: $N_x = N_y = 18$, $l_x = l_y = 6\,\text{mm}$, $\delta = l_x/8$.
  Hole size distribution (with $i = 1, ..., N_x + 1$, $j = 1, ..., N_y + 1$):

$$w_x(i, j) = 0 \ , \quad w_y(i, j) = 0 \ .$$

- "Unstretchable" sheet.
  Appearing in Fig. 1(e), Fig. S6C.
  Loading: Uniform horizontal or uniform vertical.
  Material: Natural rubber gum, 1.55 mm thick.
  Parameters: $N_x = N_y = 18$, $l_x = l_y = 6\,\text{mm}$, $\delta = l_x/8$.
  Hole size distribution (with $i = 1, ..., N_x + 1$, $j = 1, ..., N_y + 1$):

$$w_x(i, j) = (l_x - \delta)/2 \ , \quad w_y(i, j) = (l_y - \delta)/2 \ .$$

- "Graded" or "Dome" sheet.
  Appearing in Fig. 2, Fig. S9, Fig. S10, Fig. S13(a).
  Loading: Horizontal point loads at $y = y^M/2$ along the left and right boundaries.
  Material: Natural rubber gum of various thicknesses (1.55, 3.1 and 0.75 mm).
  Parameters: $N_x = 36$, $N_y = 18$, $l_x = 6\,\text{mm}$, $l_y = 2l_x$, $\delta = l_x/8$.
  Hole size distribution (with $i = 1, ..., N_x + 1$, $j = 1, ..., N_y + 1$):

$$w_x(i, j) = \frac{(l_x - \delta)}{2} \ , \quad w_y(i, j) = \frac{l_y - \delta}{2} \left| \cos \frac{j\pi}{N_y + 2} \right| \ .$$

- "Two bumps" sheet.
  Appearing in Fig. 3(a1-a2) and Fig. S4(b).
  Loading: Point loads at the four corners, directed along $\pm 5^\circ$ with respect to the horizontal.
  Material: Natural rubber gum, 1.55 mm thick.

Parameters: $N_x = 37$, $N_y = 18$, $l_x = l_y = 6\,\text{mm}$, $\delta = l_x/8$.
Hole size distribution (with $i = 1, ..., N_x + 1$, $j = 1, ..., N_y + 1$):

$$w_x(i,j) = \begin{cases} \frac{l_x-\delta}{2}\left|\cos\frac{i\pi}{(N_x+1)/2}\right| & \text{if } i < (N_x+1)/2+1 \\ \frac{l_x-\delta}{2}\left|\cos\frac{(i-(N_x+1)/2)\pi}{(N_x+1)/2}\right| & \text{if } i \geq (N_x+1)/2+1 \end{cases}, \quad w_y(i,j) = \frac{l_y-\delta}{2}\left|\cos\frac{j\pi}{N_y+2}\right| .$$

- "Flower" sheet.
  Appearing in Fig. 3(b1-b3).
  Loading: Point loads at the four corners (directed at $\pm 45^o$ with respect to the horizontal), or point loads at the centerpoints of the four edges (and perpendicular to those edges).
  Material: Natural rubber gum, 1.55 mm thick.
  Parameters: $N_x = 37$, $N_y = 37$, $l_x = l_y = 6\,\text{mm}$, $\delta = l_x/8$.
  Hole size distribution (with $i = 1, ..., N_x + 1$, $j = 1, ..., N_y + 1$):

$$w_x(i,j) = \frac{l_x-\delta}{2}\left|\cos\frac{2i\pi}{N_x+1}\right|\left|\cos\frac{2j\pi}{N_y+1}\right| , \quad w_y(i,j) = \frac{l_y-\delta}{2}\left|\cos\frac{2i\pi}{N_x+1}\right|\left|\cos\frac{2j\pi}{N_y+1}\right| .$$

- "C pattern" sheet.
  Appearing in Fig. 3(c1-c2).
  Loading: Point loads at few points along each boundary. All loads are perpendicular to the boundaries.
  Material: Natural rubber gum, 1.55 mm thick.
  Parameters: $N_x = 30$, $N_y = 30$, $l_x = l_y = 6\,\text{mm}$, $\delta = l_x/8$.
  Hole size distribution: We did not use analytical functions of i and j to create this pattern. The w_x, w_y couples we use are $w_x = (l_x - \delta)/2$ and $w_y = (l_y - \delta)/2$ outside the C, and $w_x = 0$, $w_y 0$ inside the C.

- "Bulging tube".
  Appearing in Fig. 4(a).
  Loading: Axial loads applied at the ends of the tube through 3D printed rings.
  Material: Natural rubber gum, 1.55 mm thick.
  Parameters: $N_x = 18$, $N_y = 40$, $l_x = l_y = 6\,\text{mm}$, $\delta = l_x/8$.
  Hole size distribution (with $i = 1, ..., N_x + 1$, $j = 1, ..., N_y + 1$):

$$w_x(i,j) = 0 , \quad w_y(i,j) = \begin{cases} (l_y-\delta)/2 & \text{if } j \leq 6\,|\,(j \geq 15\,\&\,j \leq 20)\,|\,(j \geq 26\,\&\,j \leq 31)\,|\,j \geq 35 \\ 0 & \text{if } (j \geq 7\,\&\,j \leq 14)\,|\,(j \geq 21\,\&\,j \leq 26)\,|\,(j \geq 32\,\&\,j \leq 34) \end{cases} .$$

- "Petal" sheet.
  Appearing in Fig. 4(b).
  Loading: Axial loads applied at the petal's extremities.
  Material: Natural rubber gum, 1.55 mm thick.
  Parameters: We used $w_x = (l_x - \delta)/2$ and $w_y = (l_y - \delta)/2$ along the petal's boundaries and in those regions that we want to remain stiff; we used $w_x = 0$, $w_y = 0$ elsewhere.

- "Plastic vase".
  Appearing in Fig. 4(c).
  Loading: Manual forming.
  Material: 0.5 mm-thick PETG sheet.
  Parameters: $N_x = 36$, $N_y = 18$, $l_x = 6\,\text{mm}$, l_y varies linearly from 6 mm at the bottom of the specimen to 18 mm at the top, $\delta = l_x/10$, $h = l_x/8$.
  Hole size distribution (with $i = 1, ..., N_x + 1$, $j = 1, ..., N_y + 1$):

$$w_x(i,j) = \frac{(l_x-\delta)}{2} , \quad w_y(i,j) = \frac{l_y-\delta}{2} - \frac{l_y-\delta}{2}\left|\cos\frac{j\pi}{2N_y+4}\right| .$$

- "No mechanism" sheet.
  Appearing in Fig. S7(a).

Loading: None.
Material: Natural rubber gum, 1.55 mm thick.
Parameters: $N_x = 18$, $N_y = 18$, $l_x = l_y = 6\,\text{mm}$, $\delta = l_x/8$.
Hole size distribution (with $i = 1, ..., N_x + 1$, $j = 1, ..., N_y + 1$):

$$w_x(i,j) = \frac{l_x - \delta}{2}\left|\cos\frac{i\pi}{N_x+2}\right| \ , \quad w_y(i,j) = \frac{l_y - \delta}{2}\left|\cos\frac{j\pi}{N_y+2}\right| \ .$$

- "Plastic dome".
  Appearing in Fig. S13(b).
  Loading: Horizontal point loads at $y = y^M/2$ along the left and right boundaries.
  Material: 0.5 mm-thick PETG sheet.
  Parameters: $N_x = 36$, $N_y = 18$, $l_x = 6\,\text{mm}$, $l_y = 2l_x$, $\delta = l_x/10$, $h = l_x/8$.
  Hole size distribution (with $i = 1, ..., N_x + 1$, $j = 1, ..., N_y + 1$):

$$w_x(i,j) = \frac{(l_x - \delta)}{2} \ , \quad w_y(i,j) = \frac{l_y - \delta}{2}\left|\cos\frac{j\pi}{N_y+2}\right| \ .$$

INFLUENCE OF THE DESIGN PARAMETERS ON THE IN-PLANE DEFORMATION OF PERIODIC SPECIMENS

To analyze the influence of the design parameters on the in-plane response of perforated sheets, we consider the cut pattern discussed in Fig. 1 as reference case. The results of this analysis are reported in Fig. S8. In Fig. S8(a),

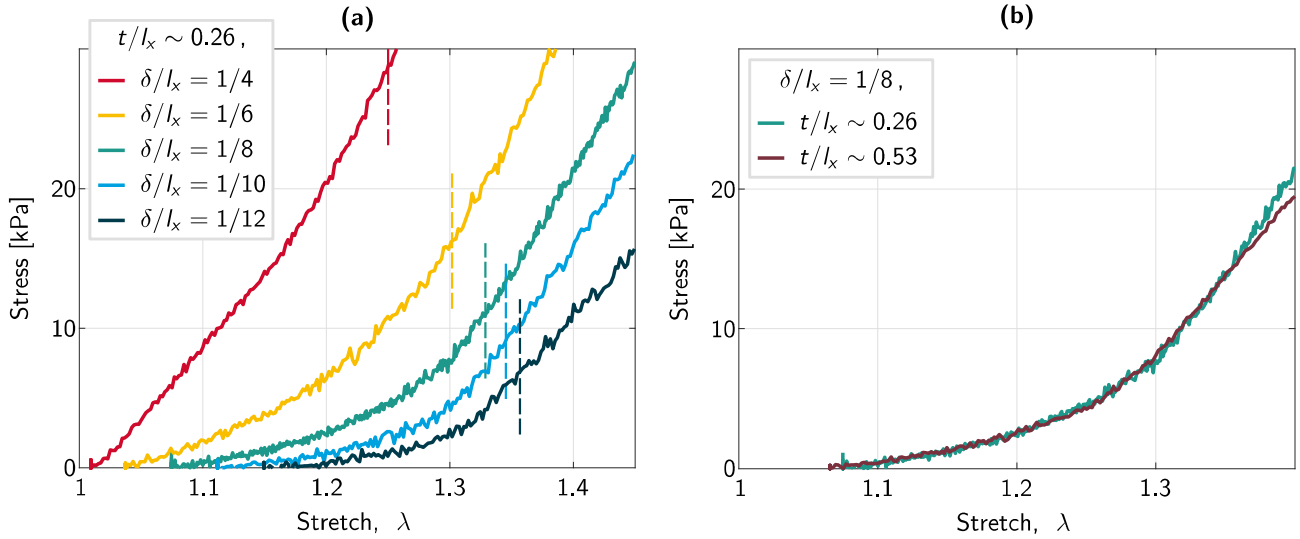

FIG. S8. (a) Dependence of the mechanism-like response on the in-plane hinge width, δ. We keep $t/l_x \sim 0.26$ constant, and we vary δ/l_x. The dashed vertical lines represent the mechanism-to-elasticity transitions for all δ/l_x cases. (b) Dependence of the mechanism-like response on the sheet's thickness, t, with $\delta/l_x = 1/8$ constant.

we show the dependence of the horizontal stretch response on the in-plane width of the hinges δ, for a constant out-of-plane thickness of the sheet $t/l_x \sim 0.26$ (corresponding to $t = 1.55\,\text{mm}$). If δ is increased, the sheet tends to lose its mechanism-like behavior. This is evident from the fact that the red and yellow continuous curves do not display a clear mechanism-to-elasticity transition. On the other hand, this transition is more pronounced for small δ. Note that the dash-dot lines represent the mechanism-to-elasticity transitions for each δ value. They are different from each other since the lengths of the tile diagonals d_h and d_v differ when we change δ.

In Fig. S8(b), we superimpose the responses of two specimens featuring the same architecture with $\delta/l_x = 1/8$, and different sheet thicknesses, t. We observe that the two responses overlap in the mechanism region, and in part of the elasticity-dominated regime. The curves deviate for stretches larger than 1.35.

INFLUENCE OF THE DESIGN PARAMETERS ON THE OUT-OF-PLANE DEFORMATION OF NON-PERIODIC SHEETS

Fig. S9 and Fig. S10 provide information on the influence of δ and t on the doming of an elastic sheet. This information is also reported in a concise way in Fig. 2(c,d). Note that these shapes have been obtained by 1) pulling the specimen by hand up to a desired stretch value, 2) nailing it to a wooden board, 3) pinching the center of the specimen to trigger out-of-plane buckling. This guarantees that all the images in Fig. S9 and Fig. S10 are obtained with consistent loading conditions. It also ensures that, if two stable solutions exist for a certain stretch value, we jump on the one that corresponds to out-of-plane deformation. For these reasons, the critical buckling stretches observed in experiments made with tensile test apparati are bound to differ from the results shown here.

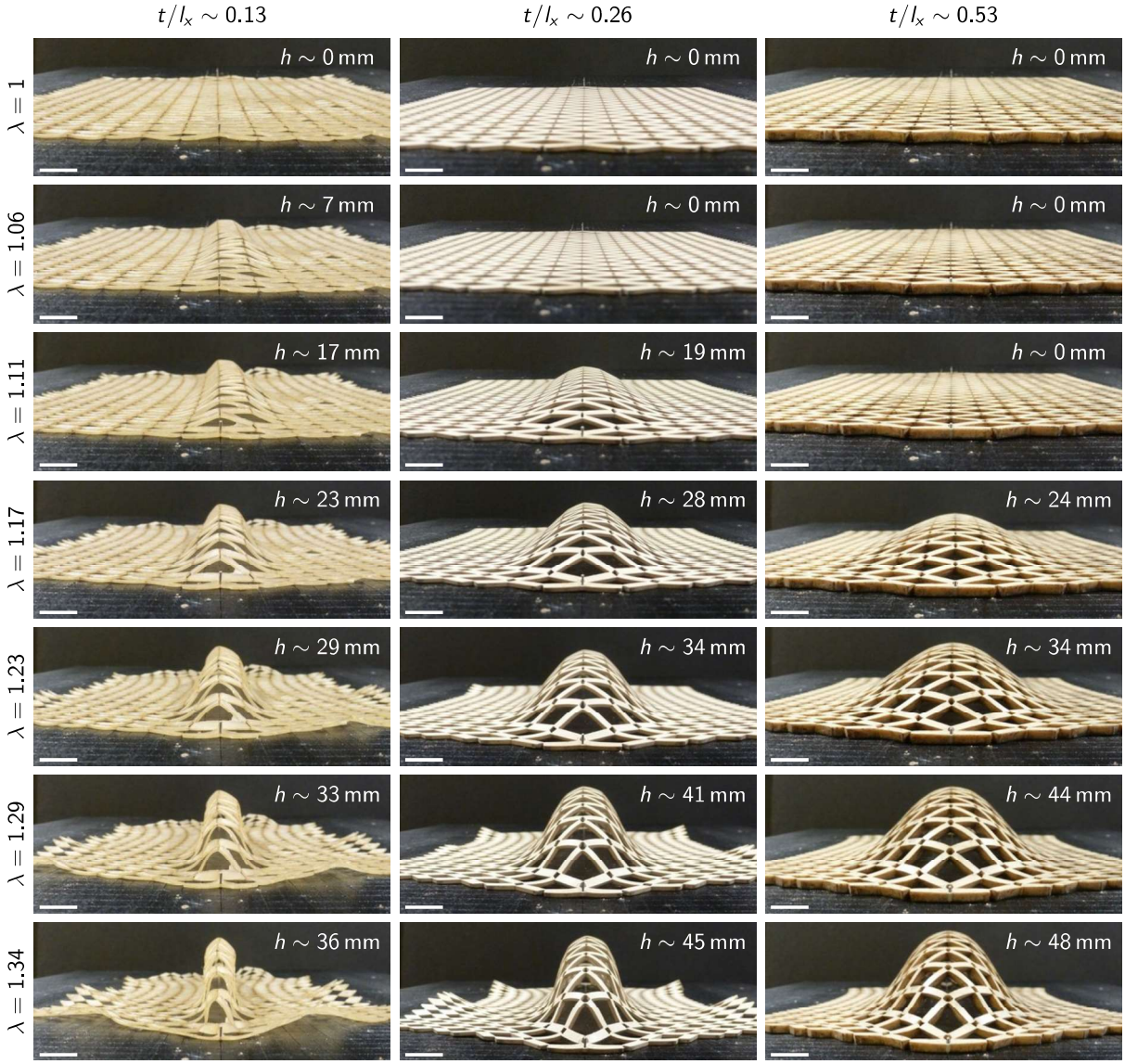

FIG. S9. Out-of-plane deformation of three graded sheets with different thicknesses, for different stretches. Rows of images correspond to specific stretch values. Columns correspond to different thicknesses of the sheets. In each image, h indicates the height of the highest point of the 3D shape with respect to its undeformed position. (Scale bar, 12 mm)

In addition to the comments in the main text, we here discuss the influence of δ/t. When t is decreased below the in-plane hinge width δ, the out-of-plane (rather than the in-plane) bending of the hinges becomes favorable: this translates into the formation of localized crease patterns [36, 38]. In our case, this behavior introduces local undulations superimposed to the global three-dimensional profile and concentrated near the loading sites. This is

shown in Fig. S10(c).

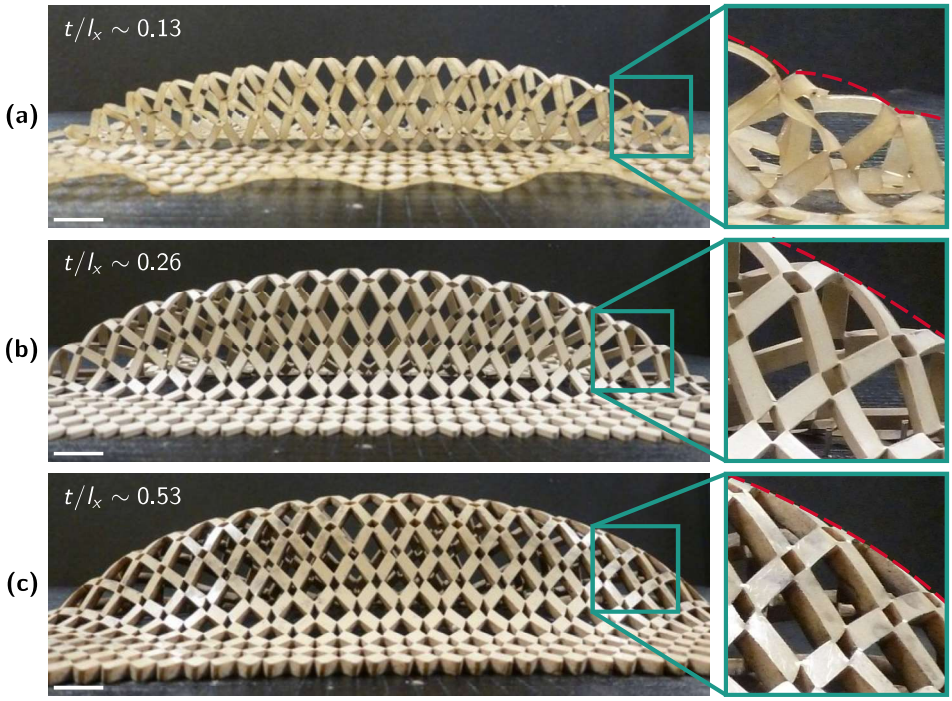

FIG. S10. Out-of-plane deformation of three graded sheets with different thicknesses, for the same stretch value. (a) Corresponds to $t/l_x \sim 0.13$, (b) to $t/l_x \sim 0.26$ and (c) to $t/l_x \sim 0.53$. The left images represent lateral views of the buckled shapes. The details highlight the local deformations of hinges and tiles near the load application points. (Scale bar, 12 mm)

LOCALIZED VS. DISTRIBUTED LOADS

All non-periodic specimens analyzed in our article have been loaded via localized boundary excitations. In this Section, we discuss the response of some of those specimens to distributed boundary loads. In Fig. S11(a), we can see the unstretched graded specimen (introduced in Fig. 2), and its deformed configuration when subjected to a uniform stretch $\lambda = 1.23$. Clearly, distributed loads do not produce any out-of-plane buckling. This is not surprising, since this

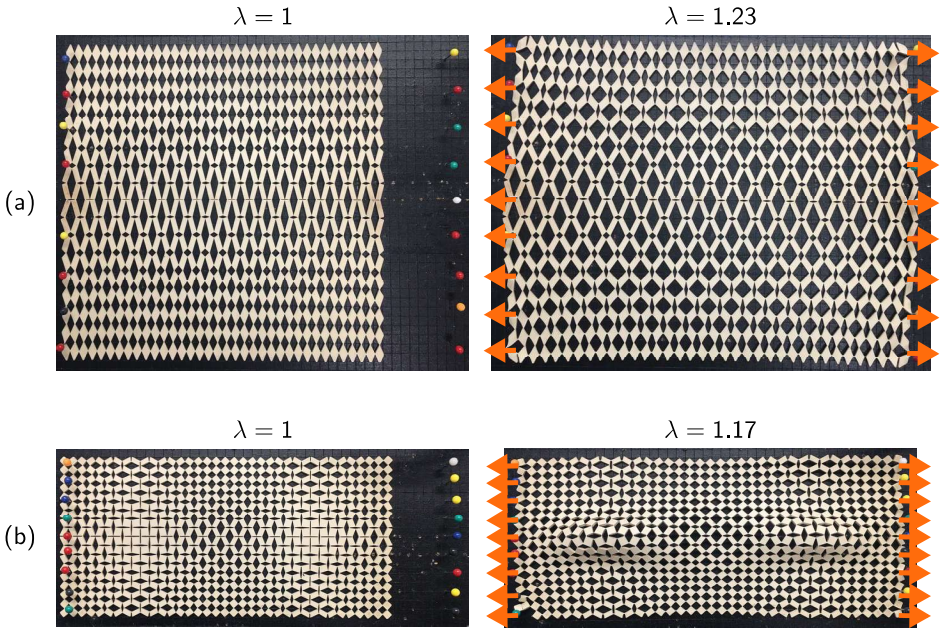

FIG. S11. (a) Deformation of the graded specimen of Fig. 2, subjected to a distributed horizontal stretch. (b) Deformation of the specimen introduced in Fig. 3a1-a2, subjected to a uniform horizontal stretch. The direction and points of application of the excitation are marked with orange arrows.

loading scenario produces a uniform stretch of each row of identical unit cells, with the central rows featuring lower stresses than the top and bottom boundary regions. In this case, no significant compressive stresses are triggered and no geometric frustration arises. In Fig. S11(b), we show the response of the specimen with two auxetic islands (introduced in Fig. 3(a1-a2) to a similar uniform load. In this case, we stretch the specimen to $\lambda = 1.17$. We can see that out-of-plane buckling occurs and that the two auxetic regions pop-up, just like in the point-loading scenario. This can be ascribed to the fact that buckling-inducing compressive stresses can still arise due to uniform loading, owing to the presence of auxetic islands surrounded by non-auxetic regions. We also notice that the buckled pattern obtained with distributed loads features bumps that are more elongated in the horizontal direction; this further proves that the loading configuration can be leveraged to control the shape of the buckled features.

ALTERNATIVE DESIGN FOR STIFF MATERIALS AND PLASTIC DEFORMATIONS

In order to fabricate sheets out of stiff materials, and to have our sheets retain their 3D shape upon load removal, we slightly modify our cut pattern design. To achieve shape retention, we leverage plastic deformations that occur at the hinges when elastic-plastic materials are used. If the same hinge geometry used for soft materials were used for stiff ones, both periodic and non-periodic specimens would shatter at the hinges when pulled open. This is why we modify our hinge design. To do so, we follow the guidelines offered by Shang, Pasini et al. [54]. This entails defining octahedra-shaped cuts instead of diamond-shaped ones at each grid point. This new design is illustrated in Fig. S12(b). It represents the compliant mechanism version of the architecture in Fig. S12(a). As a result, the hinges

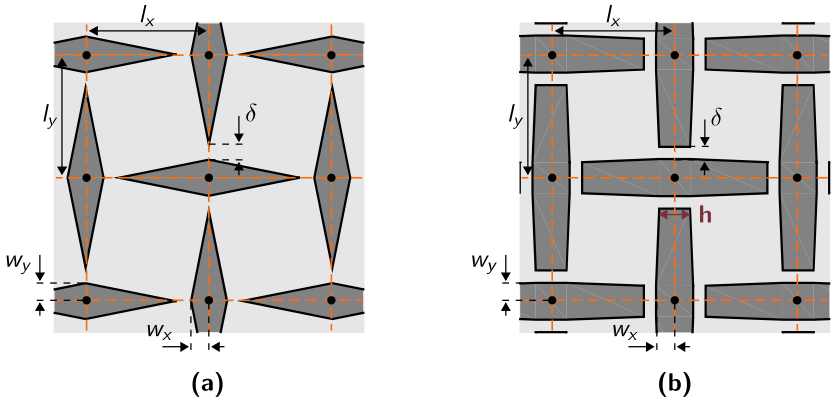

FIG. S12. An alternative design startegy for stiff materials. (a) Detail of an architecture obtained with our initial design strategy. (b) Compliant beam version of the same architecture, where we have introduced the additional parameter h, representing the in-plane hinge length.

produced with the new design have a finite length h. Note that the overall response of this alternate geometry is similar to the original one. The requirement is for the hinge length h to be much smaller than the distances between gridpoints, l_x and l_y.

In Fig. S13, we compare the response of the natural rubber sheet also shown in Fig. 3(a1), to the response of a sheet made of PETG, featuring a similar cut pattern albeit modified by selecting $\delta = l_x/10$ and introducing $h = l_x/8$. Upon load removal, the PETG sheet partially retains its deformed, three-dimensional shape, while the rubber one does not.

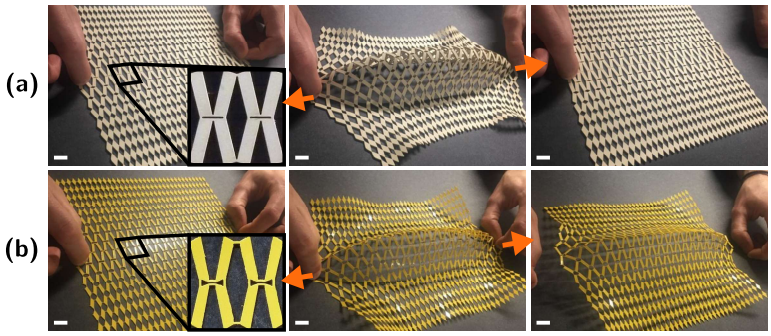

FIG. S13. (a) Three stages of the deformation of the natural rubber specimen studied in Fig. 3(a). (b) Deformation of a similar sheet, made of PETG and featuring the design variation shown in Fig. S12(b). (Scale bar, 12 mm)